Microstructure and Mechanical Properties of Fiber-Laser-Welded and Diode-Laser-Welded AZ31 Magnesium Alloy

S.M. CHOWDHURY, D.L. CHEN, S.D. BHOLE, E. POWIDAJKO, D.C. WECKMAN, and Y. ZHOU

The microstructures, tensile properties, strain hardening, and fatigue strength of fiber-laser-welded (FLW) and diode-laser-welded (DLW) AZ31B-H24 magnesium alloys were studied. Columnar dendrites near the fusion zone (FZ) boundary and equiaxed dendrites at the center of FZ, with divorced eutectic β-$Mg_{17}Al_{12}$ particles, were observed. The FLW joints had smaller dendrite cell sizes with a narrower FZ than the DLW joints. The heat-affected zone consisted of recrystallized grains. Although the DLW joints fractured at the center of FZ and exhibited lower yield strength (YS), ultimate tensile strength (UTS), and fatigue strength, the FLW joints failed at the fusion boundary and displayed only moderate reduction in the YS, UTS, and fatigue strength with a joint efficiency of ~91 pct. After welding, the strain rate sensitivity basically vanished, and the DLW joints exhibited higher strain-hardening capacity. Stage III hardening occurred after yielding in both base metal (BM) and welded samples. Dimple-like ductile fracture characteristics appeared in the BM, whereas some cleavage-like flat facets together with dimples and river marking were observed in the welded samples. Fatigue crack initiated from the specimen surface or near-surface defects, and crack propagation was characterized by the formation of fatigue striations along with secondary cracks.

I. INTRODUCTION

LIGHT weighting is one of the most important measures for cutting down greenhouse gas emissions, increasing fuel efficiency, and reducing automotive and aircraft component costs.[1–6] Advanced high-strength steels, aluminum alloys, and polymers are being used to reduce weight, but substantial reductions could be achieved by greater applications of magnesium (Mg) alloys. Mg alloys are the lightest structural metallic material with high strength-to-weight ratio and thus are attractive for use in the transportation and mobile electronics applications. Sheet forming processes of wrought Mg alloys have been used to manufacture some sheet-like components, such as door inner components and outer skins of car bodies.[7]

In the application of Mg alloys in the automotive and aircraft industries, welding and joining would inevitably be involved. A variety of welding and joining techniques has been used to join Mg alloys including tungsten-inert gas welding (TIG), metal-arc inert welding, CO_2 laser welding, and solid-state Nd:YAG laser welding.[8–21] For example, Weisheit et al.[17] carried out CO_2 laser welding of different Mg alloys and showed that most Mg alloys could be welded easily without serious defects, except AZ series and AM alloy series, which exhibited extremely high levels of porosity. Zhao and Debroy[18] investigated the formation of porosity in the AM60 Mg alloy during laser welding and concluded that hydrogen in the parent material was the main origin of porosity in the welds. They suggested remelting as a remedial measure. Sun et al.[19] evaluated TIG, CO_2, and pulsed Nd:YAG laser-welded joints of AZ31 sheet and reported that TIG welding could be used to achieve welds without defects, but they noted that coarser grain sizes in TIG welds could reduce the mechanical properties. Sun et al.[21] employed Nd:YAG laser on AZ31B Mg wrought alloy and observed that weld penetration increased by adding oxide fluxes (TiO_2, SiO_2, Cr_2O_3) on the materials to be joined. Although the as-welded fusion zone (FZ) with oxide fluxes had a deeper weld penetration, the tensile strengths of the welded joints with activating fluxes were lower because of the presence of larger grain sizes in the FZ. This was attributed to the fact that the absorptivity of laser energy increased, i.e., more energy was absorbed by the flux coat that was transmitted to the specimen in the early period of laser interaction. These observations indicated that significant microstructural changes occurred after welding, including local variations of grain size in the FZ and heat-affected zone (HAZ),

S.M. CHOWDHURY, Graduate Student, D.L. CHEN, Professor and Ryerson Research Chair, and S.D. BHOLE, Professor, are with the Department of Mechanical and Industrial Engineering, Ryerson University, Toronto, Ontario M5B 2K3, Canada. Contact e-mail: dchen@ryerson.ca E. POWIDAJKO, Graduate Student, D.C. WECKMAN, Professor, and Y. ZHOU, Professor and Canada Research Chair, are with the Department of Mechanical and Mechatronics Engineering, University of Waterloo, Waterloo, Ontario N2L 3G1, Canada.

precipitate size, shape of grains and their orientation, and formation of porosity. Such changes could affect the integrity and reliability of the welded joints and structures drastically because they would have a significant influence on the mechanical properties such as tensile and fatigue strength, ductility, and strain-hardening behavior. Therefore, the evaluation of mechanical properties in relation to the microstructural changes after welding is necessary.

The question remains as to whether a more effective welding process is available that could be used to minimize the microstructural changes and enhance the fatigue resistance of welded magnesium alloys. Recently, there has been a rapid increase in the use of fiber lasers because of their increased power density, good beam quality, and higher efficiency.[22] The fiber laser can produce a spot diameter substantially smaller than conventional lasers, thus allowing the use of longer working distances. Fiber lasers have been reported to be more cost effective than equivalent power Nd:YAG lasers when all factors such as floor space, chillers and maintenance, electrical power, *etc.*, are taken into consideration.[23] Although some limited work on the fiber laser welding (FLW) of Mg alloys has been reported recently,[24,25] no fatigue behavior of fiber-laser-welded Mg joints has been reported in the literature. It is unknown whether the fatigue resistance and other mechanical properties would be improved with the FLW. The aim of the current investigation was, therefore, to identify fatigue resistance of FLW Mg joints in comparison with diode-laser-welded (DLW) joints along with the evaluation of microstructure, tensile properties, and strain-hardening behavior.

II. MATERIAL AND EXPERIMENTAL PROCEDURE

In the current study, 2-mm-thick AZ31B-H24 Mg alloy sheet was used. The nominal chemical composition of this alloy was 2.5 to 3.5 wt pct Al, 0.7 to 1.3 wt pct Zn, 0.2 to 1.0 wt pct Mn, and balance Mg. The work pieces were sheared and then the faying surfaces were milled. Oil and other surface contaminants were removed using acetone and methanol rinse. Immediately prior to welding, preexisting surface oxides were removed with a stainless steel wire brush and then the surface was cleaned using ethanol. Butt welding was conducted without filler metal. There were two major controlling parameters in both the fiber and diode-laser-welding processes: the welding rate and power input. For the DLW process, 3 kW laser power and a welding speed of 8.33 mm/s were used, whereas for the FLW process, 2 kW laser power and a welding speed of 100 mm/s were selected as the optimal welding condition in the current study. During welding, helium was used as shielding gas. After welding, the weld quality was evaluated initially by visual observation and the samples were sectioned subsequently in the direction perpendicular to the welding direction. Then, the specimens were cold mounted, ground, and polished carefully. Two types of etchants were used.[26] Etchant 1 (10-mL acetic acid [99 pct], 4.2-g picric acid, 10-mL distilled H_2O, and 70-mL ethanol (95 pct) was used to reveal the grain boundaries, whereas etchant 2 (10-mL acetic acid (99 pct), 4.2-g picric acid, 70-mL ethanol (95 pct) was used to reveal the columnar and equiaxed dendrite solidification microstructure in the welded zone. An optical microscope coupled with a Clemex image analysis system (Clemex Technologies, Inc., Quebec, Canada) was used to observe the weld microstructures. Vickers microhardness tests were performed on the unetched samples. A load of 100 g and a dwell time of 15 seconds were used during hardness testing. All indentations were spaced adequately to avoid any potential effect of strain fields caused by adjacent indentations.

Subsized tensile specimens in accordance with ASTM E8M-08 standard[27] were machined along the rolling (or longitudinal) direction for the base metal (BM). The welded samples that were also oriented in the rolling direction were machined perpendicular to the welding direction. Tensile tests were performed at room temperature using a fully computerized universal tensile testing machine at constant strain rates of 1×10^{-2} seconds^{-1}, 1×10^{-3} seconds^{-1}, 1×10^{-4} seconds^{-1}, and 1×10^{-5} seconds^{-1}. An extensometer with a gauge length of 25 mm was used to measure the strain during the tensile tests. At least two samples were tested at each strain rate. Fatigue tests were carried out using a fully computerized Instron 8801 servo-hydraulic testing system (Instron, Norwood, MA) under load control at different stress amplitudes. A stress ratio of R ($\sigma_{min}/\sigma_{max}$) equal to 0.1, sinusoidal waveform, and frequency of 50 Hz were selected in all the tests. At each stress level, at least two samples were tested. The base metal and the welded joints after the tensile and fatigue tests were examined via a JSM-6380LV scanning electron microscope (SEM) equipped with Oxford energy dispersive X-ray spectroscopy (EDS) system and three-dimensional fractographic analysis capacity.

III. RESULTS AND DISCUSSION

A. *Microstructure*

During laser welding, energy can be transferred from the laser to the material to be welded in two ways or modes. Depending on the power density, the laser welding can be in either keyhole mode or conduction mode, as shown schematically in Figure 1 for the FLW and DLW joints, respectively. The keyhole welding melts a keyhole or hole in the material being welded because of the higher energy density (such as FLW) delivered to the material, and as the beam moves forward, the molten metal fills in behind it. However, conduction welding is a lower energy density weld (such as DLW) in which the laser beam basically heats the surface of the material being welded and the heat is transferred gradually to the bottom of the material through heat-conduction and advection of the fluid in the weld pool.

Photographs of the top weld beads after FLW and DLW appeared to be good after complete cleaning of

the oxides, as can be observed from Figures 2(a) and (b), respectively. Because of solidification shrinkage and thermal contraction of the weld metal during welding, the workpiece had a certain tendency to distort. Because of the deep narrow keyhole in FLW, the weld bead was narrow both at the top and the bottom, and no distortion was observed. However, the DLW workpiece was more or less shrunk in the upward direction. In this case, the weld tended to be wider at the top than at the bottom, causing more solidification shrinkage and thermal contraction at the top of the weld than at the bottom with drop-through or sagging of the large weld

pool. Consequently, the resultant angular distortion looked like a negative meniscus shape and the concave shape faced somewhat upward.[28] Figures 3 and 4 show the typical microstructure of the fiber and diode laser-welded joints. To identify better the grain structure and dendrites in the FZ of the laser-welded joints, two different kinds of etchants were employed individually in the current study. Etchant 1 (with water) was used to reveal the grain structure as shown in Figure 3(d), (f), (c), (e), while etchant 2 (without water) was used to reveal the dendrites only (Figures 3(e), (g), (d), and (f)). Water was a key ingredient that made the difference between those two etchants. When etching took place, the etchant with water (etchant 1) preferentially attacked the high-energy grain boundaries. It is observed that the fusion boundary of FLW joint had a slight hourglass shape (Figure 3(a)), whereas the DLW joint was featured by a weld drop-through (caused during welding because of the weight of the molten Mg) (Figure 4(a)) with an almost hemispherical shape. In Figure 3(b), elongated and pancake-shaped grains with varying sizes were observed in the BM. The heterogeneity in the grain structure of the BM was a result of both deformation of the 2-mm-thick sheet by rolling and incomplete dynamic recrystallization (partial annealing).[29] The average grain size of the BM was observed to be 3.6 ± 2.2 μm. Equiaxed grains were observed in the HAZ in both types of laser-welded joints as shown in Figure 3(c) and Figure 4(b), which suggests that recrystallization occurred in the HAZ. Figures 3(d), 3(e), and 4(c) depict the columnar grains along with columnar dendrites adjacent to the solid–liquid boundary or fusion line. It is observed that epitaxial growth of the columnar grains was almost perpendicular to the boundary of the fusion line because of the large thermal gradients. Savage et al.[30] first observed epitaxial grain growth in fusion welding using the Laue X-ray back reflection technique and pointed out that the existing BM grains at the fusion line acted as the substrate for nucleation. Because the liquid metal of the weld pool was in intimate contact with these substrate grains and wetted them completely, crystals nucleated from the liquid metal on the substrate grains without alternating their existing crystallographic orientations. Similarly, Xiao et al.[31] observed that during laser welding, weld pool solidification always started from the parent metal
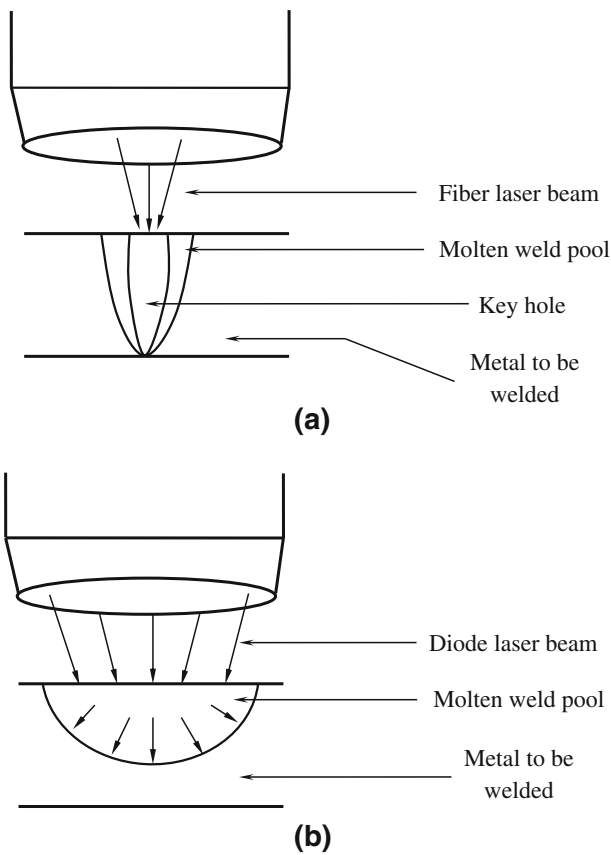

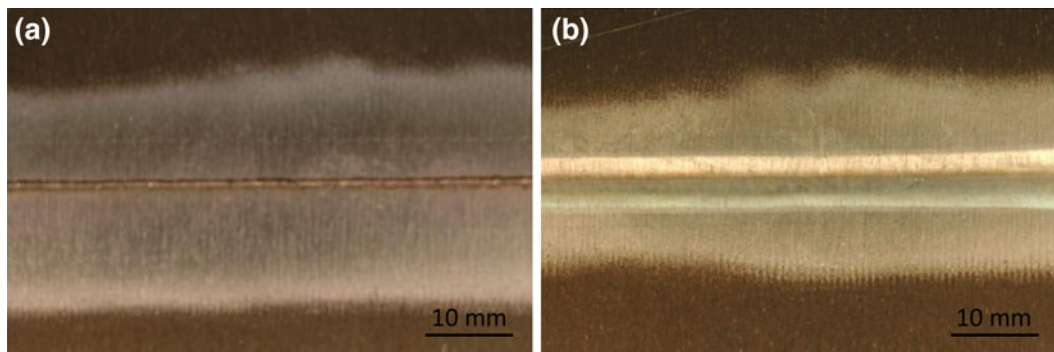Fig. 1—Schematic illustration of (a) keyhole and (b) conduction modes during laser welding.

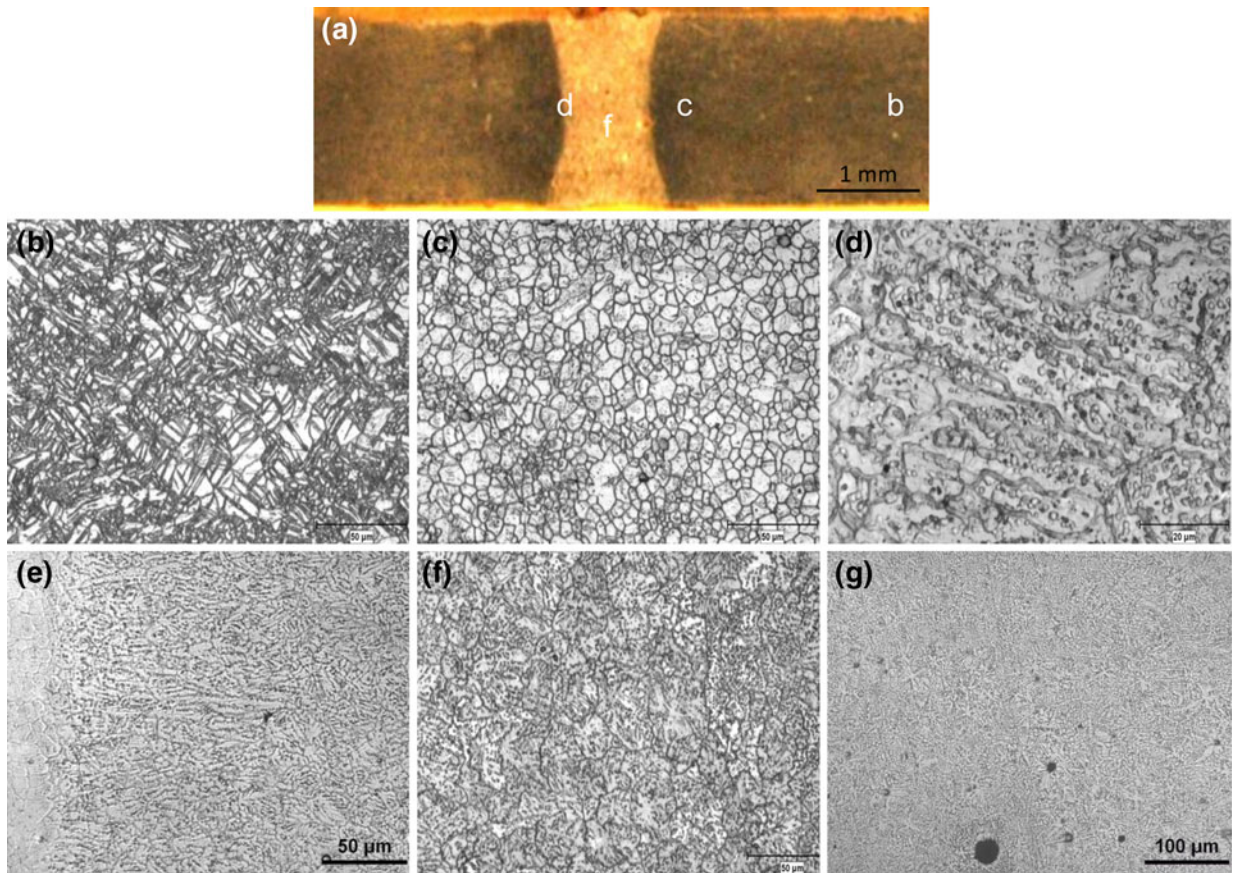Fig. 2—Top weld bead of (a) fiber laser-welded joints and (b) diode laser-welded joints.

Fig. 3—Typical microscopic structures of fiber laser-welded joint at a welding speed of 100 mm/s. (*a*) cross section of the welded joint, (*b*) base metal (BM) (etchant 1), (*c*) heat-affected zone (HAZ) at 400 times magnification (etchant 1), (*d*) columnar dendrites near the boundary of fusion zone (FZ) at 1000 times magnification (etchant 1), (*e*) columnar dendrites at 400 times magnification (etchant 2), (*f*) FZ at 400 times magnification (etchant 1), and (*g*) FZ at 200 times magnification (etchant 2).

partially molten zone with a minimum degree of undercooling because the solidification phase has the same crystalline structure with the BM. This led to the well-known epitaxial growth without requiring any nucleation event.

During the solidification of an alloy, the temperature gradient at the solid–liquid interface G and the growth rate R played a crucial role to produce the planar, cellular or dendritic microstructure in the FZ. The ratio of G/R determined the mode of solidification (planar, columnar, or equiaxed dendrites), whereas the product of $G \times R$ indicated the cooling rate that governed the size of the solidification structure. Several papers have been published to identify the effect of G and R on the microstructure in the FZ.[31–36] To facilitate a better understanding of the effect of G/R and $G \times R$ on the morphology and size of solidification microstructures, a schematic plot is shown in Figure 5.[37] It is observed that the moderate temperature gradient at the boundary of fusion line resulted in columnar dendrites in both welded joints, whereas in the center of the FZ, dendrites became equiaxed because of a lower temperature gradient. As FLW had a higher cooling rate, both the columnar and equiaxed dendrites were observed to be small in comparison with the DLW joint. However, bubble formation was observed during FLW, which will

be better observed on the fracture surface in the later section. Bubbles were generated from the tip of the keyhole and then rotated at the bottom portion of the molten pool just behind the keyhole, as shown schematically in Figure 6. The bubbles trapped at the solidifying front of the FZ resulted in the formation of porosity, as also observed in Reference 38.

It is of interest to observe some dark second-phase particles as sites of heterogeneous nuclei at the center of equiaxed grains in the FZ of the DLW joints, as shown in Figure 4(g). A similar type of heterogeneous nuclei was observed in the FLW joints at a higher magnification of the SEM image (Figure 7(a)), where an EDS analysis revealed that these particles were the unmelted BM Mn-Al containing inclusions that were still present in the weld pool to block off the epitaxial columnar grains and act as heterogeneous nuclei on which atoms in the liquid metal could be arranged in a crystalline form. It is observed from Figures 3(g) and 4(f), which were taken at the same magnification after etching with the same etchant (etchant 2), that smaller grains along with Mn-Al particles positioned at the center of the equiaxed dendrite cells were apparent in the FLW joint in comparison with the DLW joint, because of the much higher cooling rate during FLW arising from (1) the much narrower FZ or weld pool
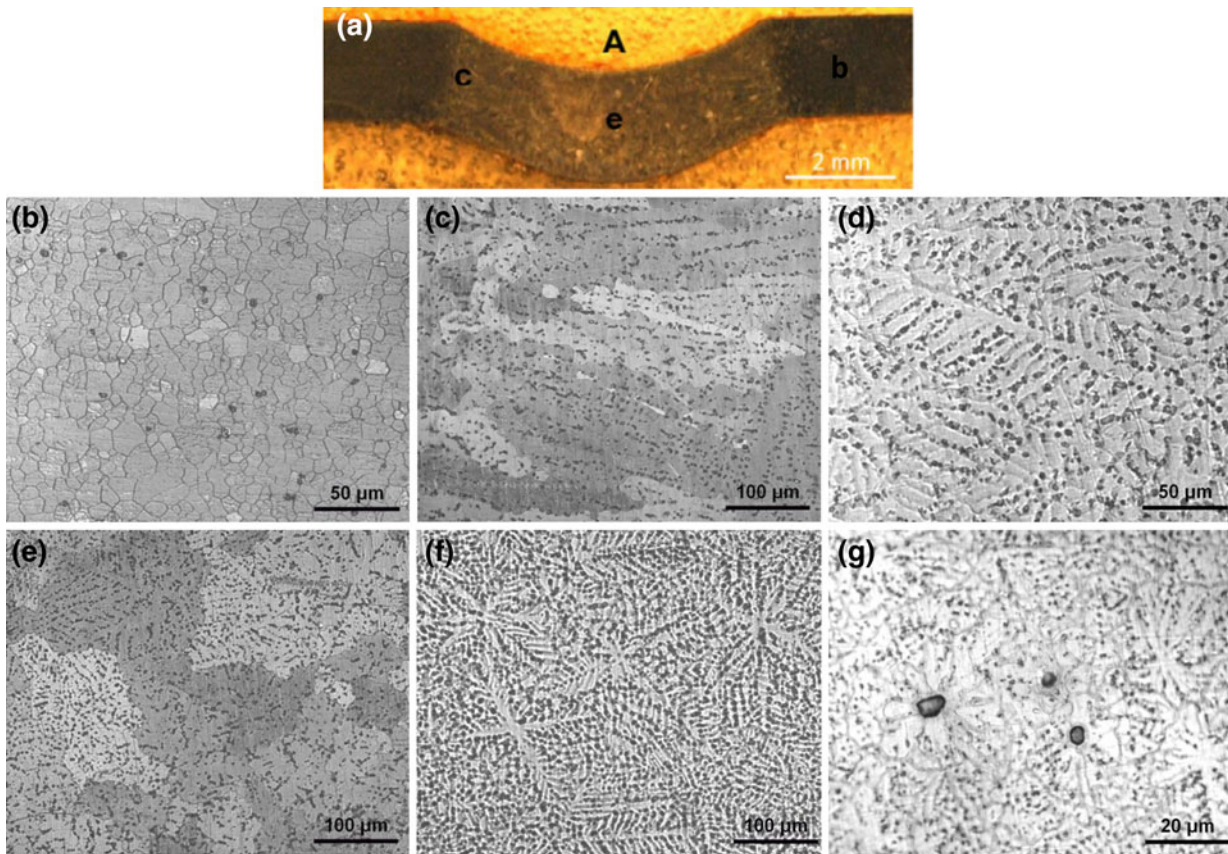
Fig. 4—Typical microscopic structures of a diode laser-welded joint at a welding speed of 8.33 mm/s. (*a*) cross section of the welded joint, (*b*) HAZ at 400 times magnification (etchant 1), (*c*) columnar dendrites at 200 times magnification (etchant 1), (*d*) columnar dendrites at 400 times magnification (etchant 2), (*e*) fusion zone (FZ) at 200 times magnification (etchant 1), (*f*) FZ at the same magnification (etchant 2), and (*g*) heterogeneous nuclei in the FZ (etchant 2).
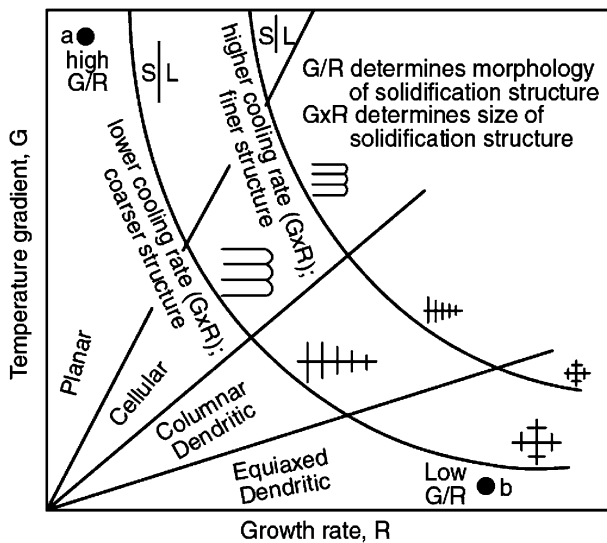

Fig. 5—Effect of temperature gradient *G* and growth rate *R* on the formation of various solidification microstructures[37].

Fig. 6—Schematic illustration of bubble formation in the FZ of the fiber laser-welded joint.

(Figure 3(a) *vs* Figure 4(a)) and (2) the over 10 times faster welding speed (100 mm/s *vs* 8.33 mm/s). Similar results were observed in Reference 31 where the more and coarser the Mn-Al particles, the more efficient the
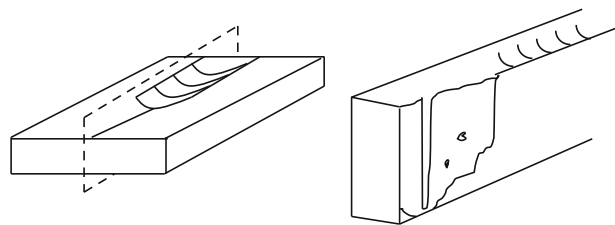
nucleation and the more grain refining of the weld. EDS analysis indicated that a large number of precipitates was present in conjunction with Mn-Al particles/inclusions in both types of laser-welded joints. As observed from Figure 7(b), a divorced eutectic β-$Mg_{17}Al_{12}$ particle on the left hand-side (without manganese) was present along with an unmelted Mn-Al particle on the right-hand side in the FZ of the DLW joint, although both particles had the similar white color on the image. The presence of the divorced eutectic structure was caused by the fast nonequilibrium cooling of the weld pool during welding, because no normal eutectic structure in the form of alternating layers of α-μg and β-$Mg_{17}Al_{12}$ would be possible in the AZ31 Mg alloy containing only 3 wt pct Al based on the equilibrium
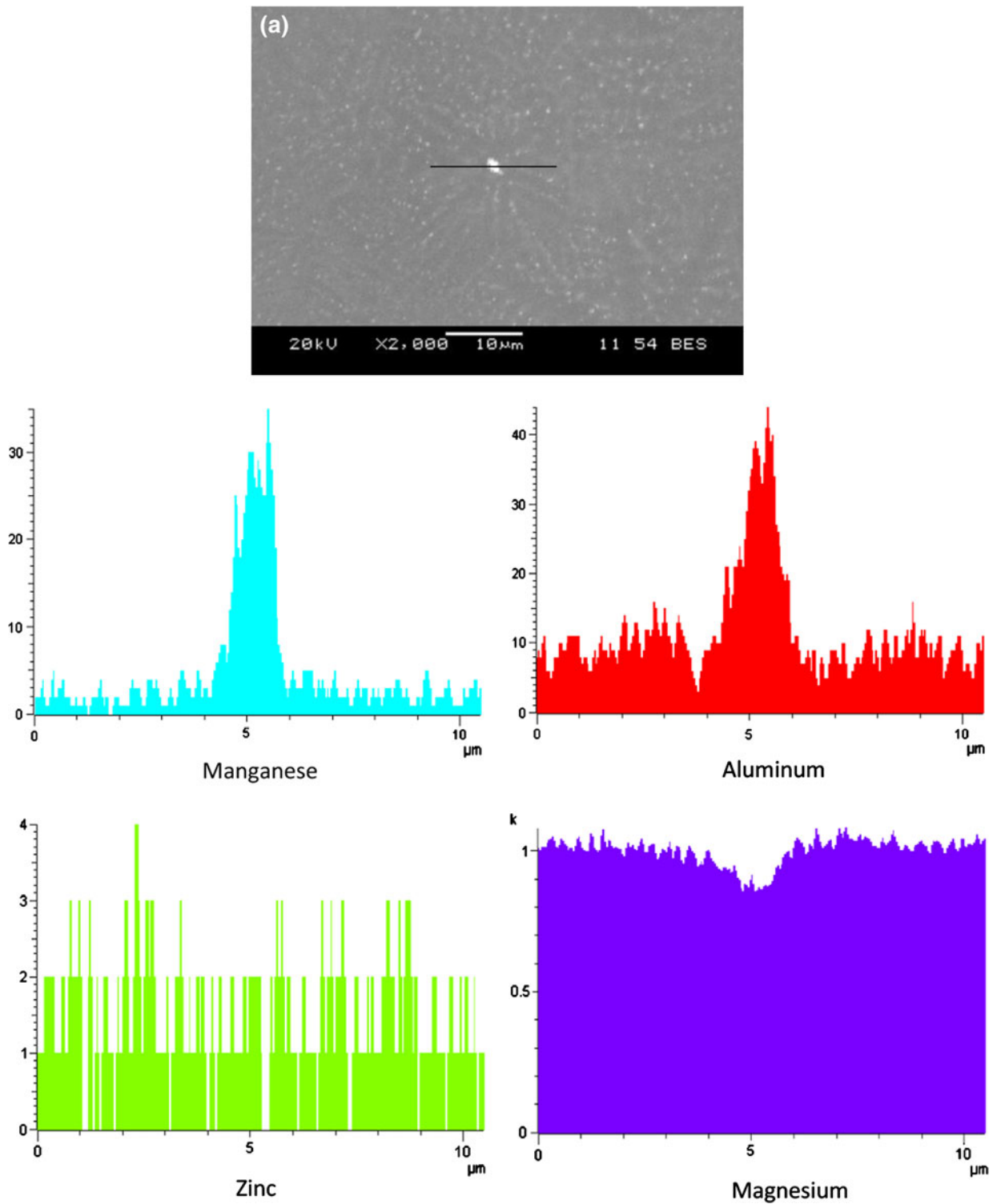
Fig. 7—EDS line scan showing the typical compositional variation (*a*) across a particle in the FZ of FLW joint and (*b*) across two particles in the FZ of DLW joint.

phase diagram if the cooling rate would be infinitely slow (*i.e.*, under equilibrium cooling). Such β-$Mg_{17}Al_{12}$ precipitates were also observed in the FZ of laser/arc hybrid[39]; TIG[40]; electron beam[41]; gas tungsten arc[42]; and double-sided arc-welded[43] Mg joints.

B. *Microhardness*

Typical hardness profiles across the FLW and DLW AZ31B-H24 Mg alloy are shown in Figure 8. It is observed that the lowest hardness value appeared in the
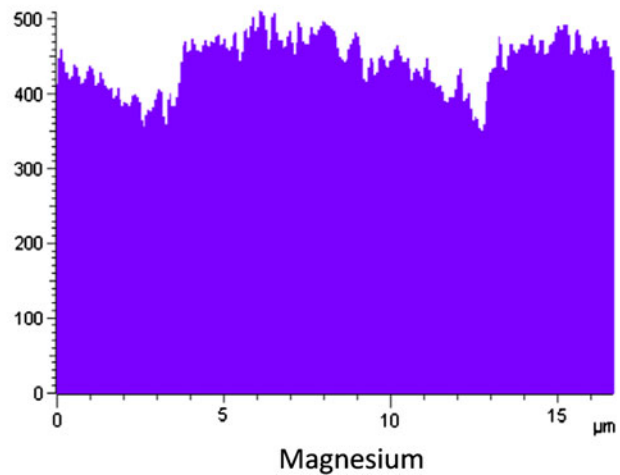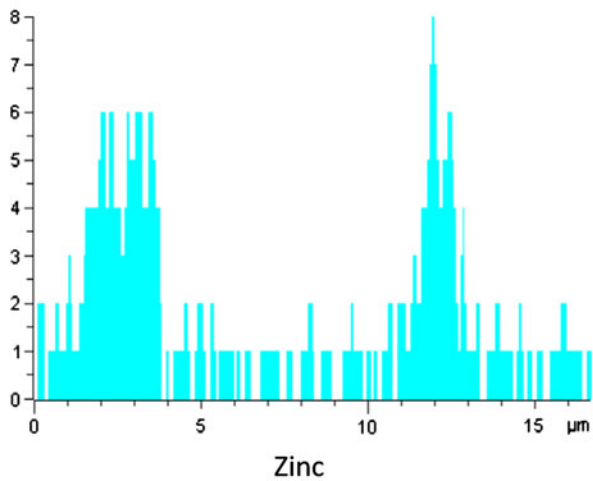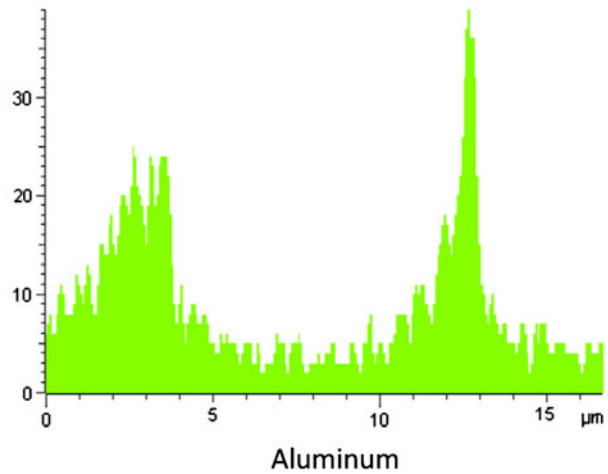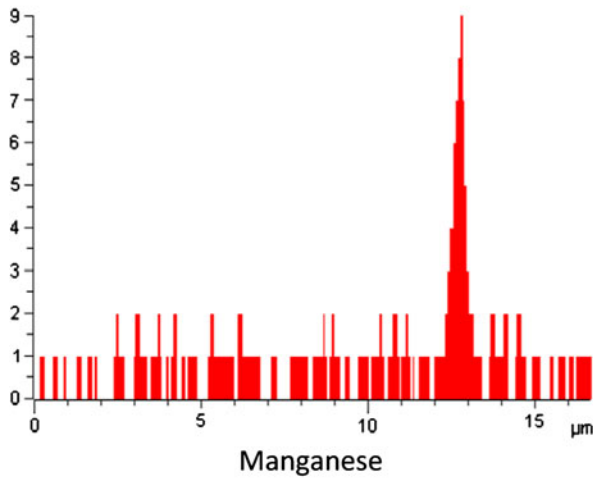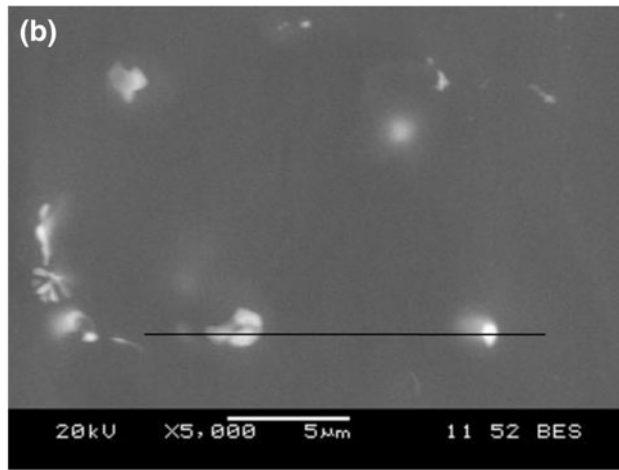
Fig. 7—Continued.

FZ in both types of laser welding. The hardness value decreased from approximately HV 73 to 74 in the half-hardened H24 temper BM to approximately HV 53 at the center of the FZ, indicating narrow FZ and HAZ in the FLW joint (Figure 8(a)). However, in the DLW joint, much wider FZ and HAZ were obvious (Figure 8(b)). Besides, the lowest hardness of the DLW joint became about HV 45, which was lower than that of the FLW joint. This was associated with the faster cooling rate during the FLW because of the smaller amount of weld pool (Figure 3(a)) and faster welding speed compared with the DLW, leading to a smaller grain size in the FZ (Figures 3(e) through (g)). The overall reduction in the hardness after laser welding was
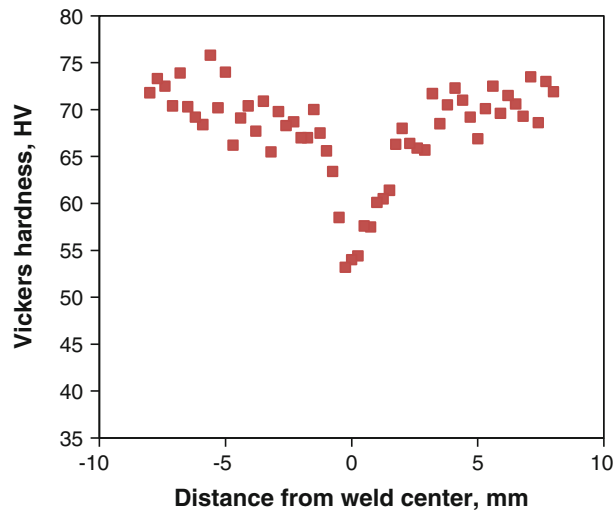
(a)
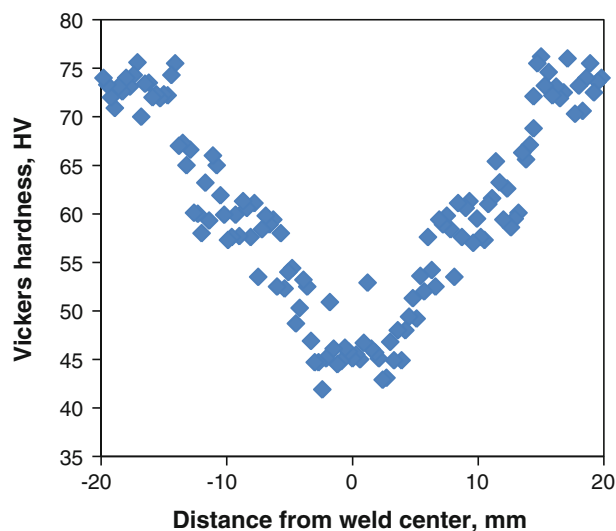
(b)

Fig. 8—Typical microhardness profile of (*a*) fiber laser-welded joint at a welding speed of 100 mm/s and (*b*) diode laser-welded joint at a welding speed of 8.33 mm/s.

attributed to the significant microstructural changes. In the FZ (Figures 3(e) through (g)), the nonequilibrium cast structures formed with a larger grain size in the FZ than that of the BM (Figure 3(b)). Furthermore, the grain shape had a significant change from the deformed and elongated (or pancake-shaped) grains in the half-hardened H24 condition (Figure 3(b)) to the fully annealed or recrystallized equiaxed grains in the HAZ (Figures 3(c) and 4(b)), to the characteristic dendrite cells with divorced eutectic structures as described previously. All these factors contributed to the hardness change shown in Figures 8(a) and (b).

C. Tensile Properties

Figure 9 shows typical engineering stress–strain curves of the BM, FLW, and DLW AZ31 Mg alloy
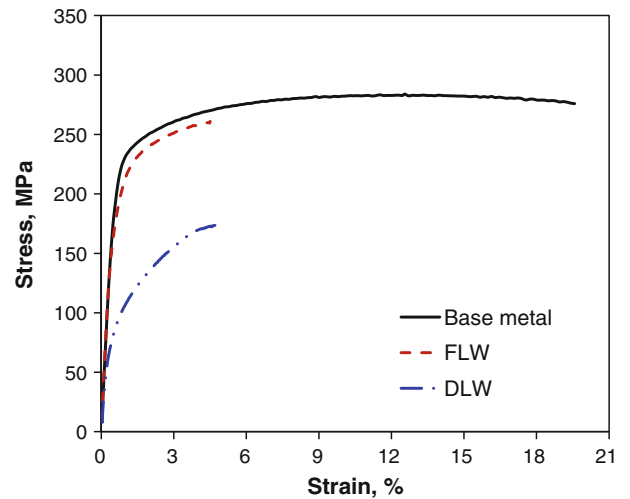

Fig. 9—Typical engineering stress–strain curves of the AZ31B-H24 Mg alloy, fiber laser-welded and diode laser-welded samples tested at a strain rate of 1×10^{-4} s^{-1}.

sheets tested at a strain rate of 1×10^{-4} seconds^{-1}. It is observed that after welding, both the strength and the elongation (pct El) were reduced. A joint efficiency was observed to be about 91 pct for the FLW joint and 59 pct for the DLW joint. The significant reduction of the tensile strength for the DLW joint would be related to the larger grains (dendrite cells) in the FZ (Figures 4(e) and (f)) and irregular shape (weld sagging or drop-through, Figure 4(a)) of the weld bead that reduced the load-bearing capability during tensile testing. As described previously, the weld exhibited a typical cast dendritic structure containing a large number of brittle divorced eutectic β-Mg$_{17}$Al$_{12}$ precipitates (Figures 4(e) through (g)), which was different from the microstructure of the rolled and partially annealed BM (Figure 3(b)). As a consequence, the ductility of the AZ31B-H24 Mg alloy after laser welding reduced notably. All FLW joints fractured at the boundary of HAZ and columnar dendrites (Figure 3(e)), whereas DLW joints fractured almost exclusively at the center of the FZ. From Figure 10, it was observed that the yield strength (YS) and ultimate tensile strength (UTS) of the FLW joints, which were fairly close to those of the BM, were much higher than those of the DLW joints, although the ductility of both types of laser-welded joints was essentially the same at different strain rates. As the strain rate increased, the YS and UTS of the BM increased only slightly, but the ductility decreased drastically. This means that the BM was strain rate sensitive to a certain extent, although it was basically absent in both types of welded joints. This is because of the presence of smaller elongated grain structure in the BM, as shown in Figure 3(b). The detail of the strain rate sensitivity in relation to the grain structure has been discussed in Reference 43, and also reported by del Valle and Ruano[44] and Prasad and Armstrong.[45] The result on the small effect of strain rate in both welded joints was in agreement with those observed in Mg–9Li–1Y,[46] cryo-rolled Cu,[47] and AZ31B alloys.[29]
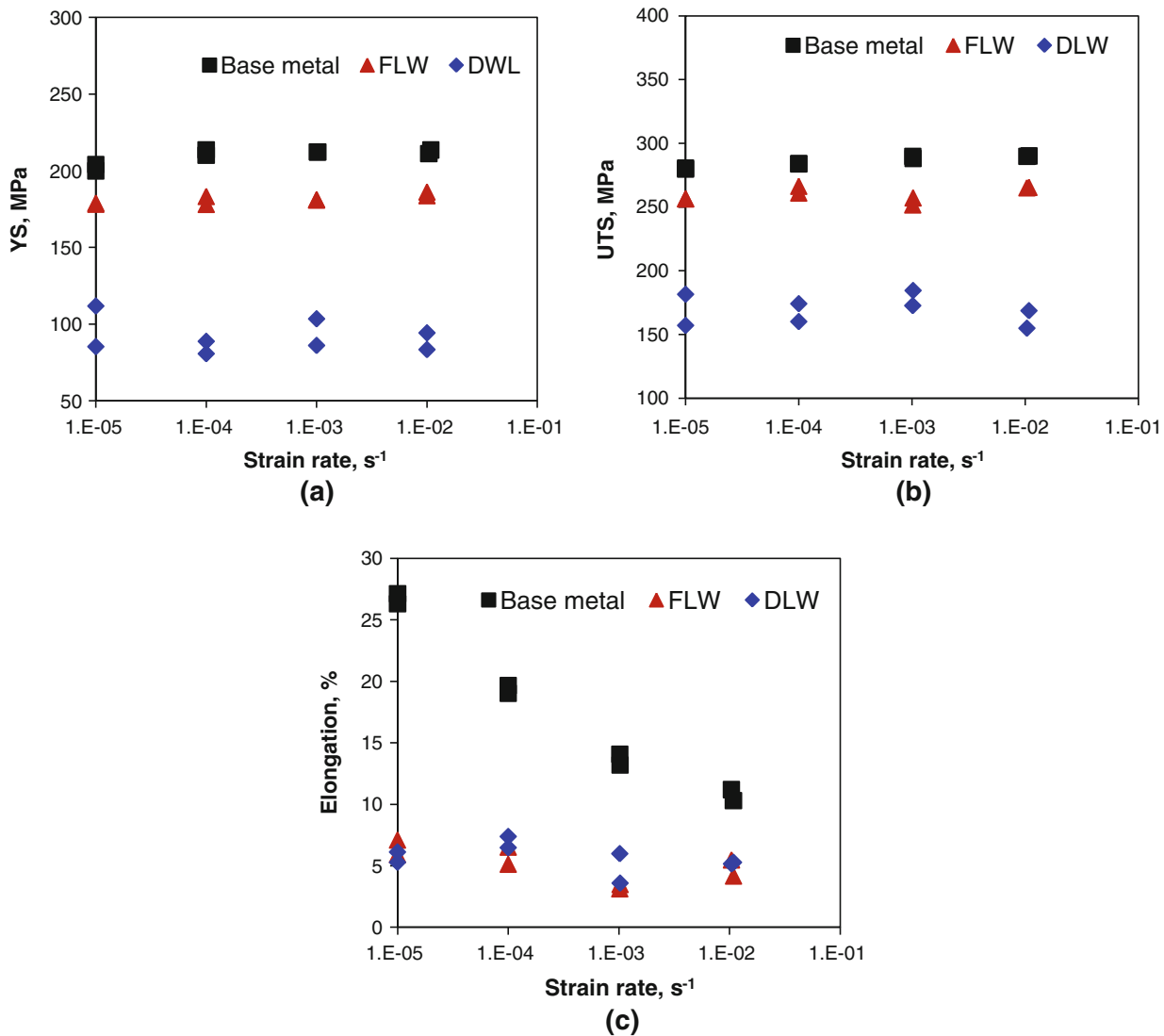
Fig. 10—Effect of strain rate on (*a*) YS, (*b*) UTS, and (*c*) ductility of the FLW and DLW samples.

D. *Strain Hardening Behavior*

The hardening capacity of a material may be considered as a direct ratio of the UTS to the YS,[48] but Afrin et al.[49] redefined the hardening capacity H_c as a normalized parameter

$$H_c = \frac{\sigma_{\mathrm{UTS}} - \sigma_y}{\sigma_y} = \frac{\sigma_{\mathrm{UTS}}}{\sigma_y} - 1 \qquad [1]$$

The obtained hardening capacity of the BM and the welded samples is listed in Table I. It is observed that the hardening capacity of the DLW joint increased more than twice that of the BM, whereas the FLW joint showed only a slight increase in the hardening capacity.

To understand the strain-hardening characteristics, it is necessary to evaluate the strain-hardening exponent, because it is a measure of the ability of a metal to strain hardening; the larger its value, the greater the strain

Table I. Hardening Capacity of the AZ31B-H24 Mg Base Alloy, FLW, and DLW Samples Tested at Different Strain Rates

Specimen	Strain Rate (s^{-1})	Hardening Capacity
Base metal	1×10^{-2}	0.37
	1×10^{-3}	0.36
	1×10^{-4}	0.36
	1×10^{-5}	0.41
FLW	1×10^{-2}	0.43
	1×10^{-3}	0.41
	1×10^{-4}	0.46
	1×10^{-5}	0.44
DLW	1×10^{-2}	0.83
	1×10^{-3}	0.90
	1×10^{-4}	0.98
	1×10^{-5}	0.73

hardening for a given amount of plastic strain. Several equations have been proposed to evaluate the strain-hardening exponent. Hollomon[50] proposed the following expression

$$\sigma = K\varepsilon^n \qquad [2]$$

where n is the strain-hardening exponent, K is the strength coefficient, σ is the true stress, and ε is the true strain. To quantify the strain-hardening response more accurately, Afrin et al.[49] proposed the following equation using the net flow stress and the net plastic strain of a material after yielding,

$$\sigma = \sigma_y + K^*\left(\varepsilon - \varepsilon_y\right)^{n^*} \qquad [3]$$

where n^*, σ, ε, σ_y, and ε_y are the strain-hardening exponent, true stress, true strain, yield strength, and yield strain of the material to be evaluated, respectively. K^* is the strength coefficient that reflects the increment in strength because of strain hardening corresponding to $(\varepsilon - \varepsilon_y) = 1$. Figure 11 presents the evaluated strain-hardening exponents (n and n^*) as a function of strain rate for the BM, FLW, and DLW joints. Only the data lying in between the YS and UTS were used to evaluate the value of n and n^*. Although almost no effect of strain rate on the strain-hardening exponents was observed within the experimental scatter, it was clear that the strain-hardening exponents after DLW became much higher because of the significant microstructural change (Figure 4), in agreement with the results of hardening capacity shown in Table I. The values of n^* were more than twice larger than those of n, suggesting that the redefined n^* exponent was more sensitive because of the exclusion of elastic deformation amount in the evaluation of n^* value expressed by Eq. [3].

To explain the strain-hardening behavior, it is necessary to take into account both grain size and dislocation hardening effects. A recent strain-hardening model considered both aspects[44,51]

$$\sigma = \sigma_o + \sigma_{HP} + \sigma_d \qquad [4]$$

where σ_o is the frictional contribution, $\sigma_{HP} = kd^{-1/2}$ is the Hall-Petch contribution, and $\sigma_d = M\alpha Gb\rho^{1/2}$ is the Taylor dislocation contribution (where G is the shear modulus, b is the Burgers vector, M is the Taylor factor, and α is a constant). Sinclair et al.[52] pointed out that, at lower strains with decreasing grain size d, the Hall-Petch contribution increased because of dislocation–grain boundary interactions, and the influence of the grain size on the strain hardening disappeared at higher strains as a result of dislocation screening and dynamic recovery effects at grain boundaries. Because the BM had a smaller grain size coupled with its predeformed/elongated grain structure, the Hall-Petch contribution (σ_{HP}) in Eq. [4] would be stronger at lower strains or in the initial hardening stage after yielding, leading to a higher strain-hardening rate in comparison with the welded joints as shown in Figure 12. This figure represents a typical Kocks-Mecking plot where stage III hardening (characterized by a linear decrease of strain-hardening rate with increasing net flow stress)
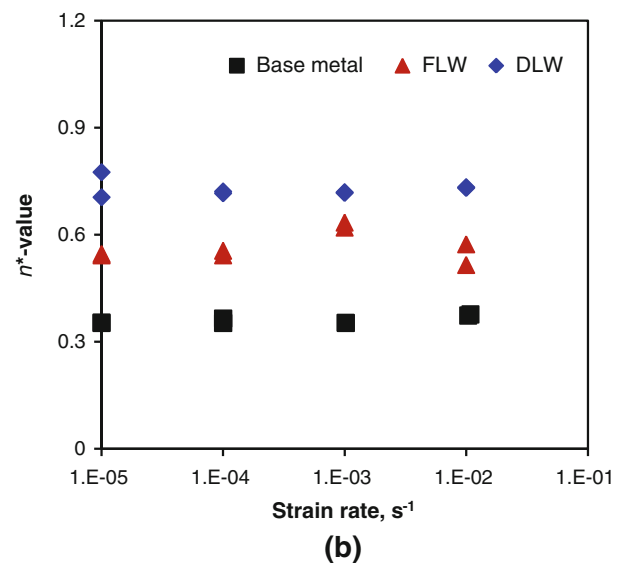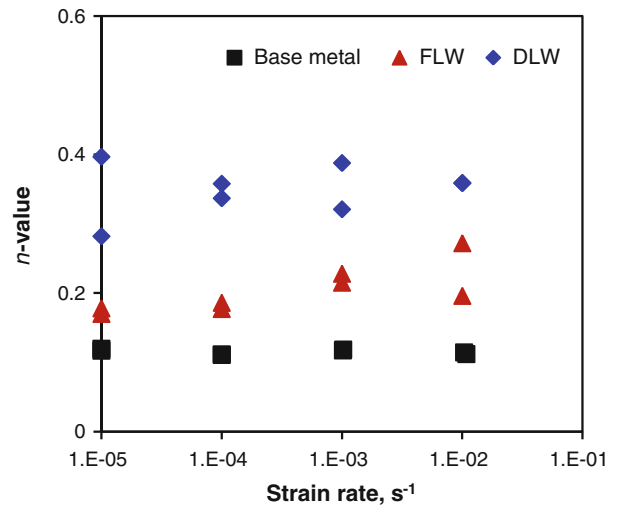

Fig. 11—Effect of strain rate on the strain-hardening exponent (a) n value and (b) n^* value in the FLW and DLW samples.

occurred immediately after yielding. As the DLW joint had a larger size of grains or dendrite cells (Figure 4(e) and (f)), it gave rise to an initially lower strain-hardening rate in stage III hardening. Pantleon[53] reported that stage III hardening was extended to stage IV via the incorporation of excess dislocations related to the disorientations, and the strain-hardening rate often remained constant or at a low level in this stage as shown in Figure 12.

At larger strains, the influence of the grain size on the strain hardening was assumed to be vanished as a result of dislocation screening and dynamic recovery effects at grain boundaries.[52,54] Near the end of stage III in Figure 12, the strain hardening of a material would be related to the dislocation strain field interactions. Stress contribution from the dislocation density can be obtained from the Taylor dislocation contribution[51,55]

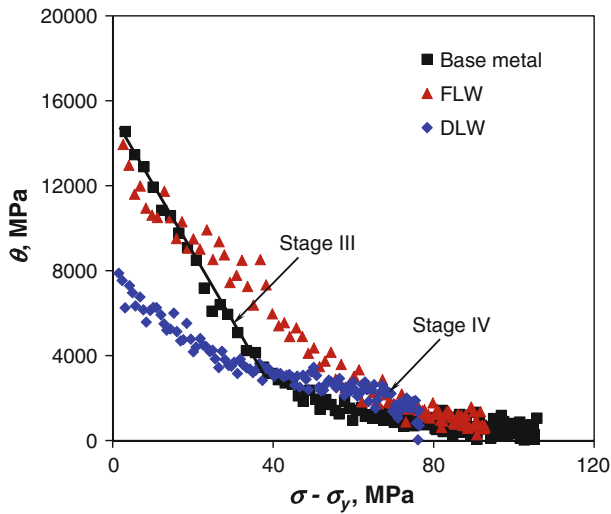$$\sigma_d \approx \sigma - \sigma_y \propto \sqrt{\rho} \qquad [5]$$

Fig. 12—Strain hardening rate (θ) *vs* net flow stress ($\sigma - \sigma_y$) of the FLW and DLW samples tested at a strain rate of 1×10^{-3} s^{-1}.

Fig. 13—S-N curves of the AZ31B-H24 base metal, FLW and DLW joints tested at $R = 0.1$, 50 Hz, and room temperature.

where ρ is the dislocation density. The net flow stress ($\sigma - \sigma_y$) necessary to continue deformation of a material was proportional to the square root of the dislocation density. The slope of the dislocation density in a metal increased with deformation or cold work because of dislocation multiplication or the formation of new dislocations, which decreased the spacing among dislocations and their interactions became repulsive. The net result would be that the motion of a dislocation was impeded by other dislocations. As the dislocation density increased, the resistance to dislocation motion by other dislocations became more pronounced. As shown in Figures 4(e) and (f), the larger dendrite cell/grain size of the DLW sample would provide more space to accommodate dislocations and increase the dislocation storage capacity, so that a relatively higher strain-hardening rate was capable of maintaining in stage IV after DLW, as shown in Figure 12. This corresponded well to the higher strain-hardening capacity (Table I) and larger strain-hardening exponent (Figure 11) in the DLW joints.

E. Fatigue Properties

Load-controlled fatigue tests were conducted on the BM, FLW, and DLW specimens, and the obtained results are shown in Figure 13. This allows a direct comparison and gives an indication of the influence of the welding on the fatigue life and integrity, which have to be taken into account in designing welded structural components made from Mg alloys. It is observed from Figure 13 that the fatigue life decreased after welding. However, similar to the yield strength and ultimate tensile strength (Figure 10(a) and (b)), the fatigue strength or life of the FLW joints was close to that of the BM, which was much higher than that of DLW joints. As the stress amplitude decreased, the difference of fatigue life among the welded joints and the BM became smaller in the semilog scale diagram. The obtained fatigue limit (defined as the fatigue strength
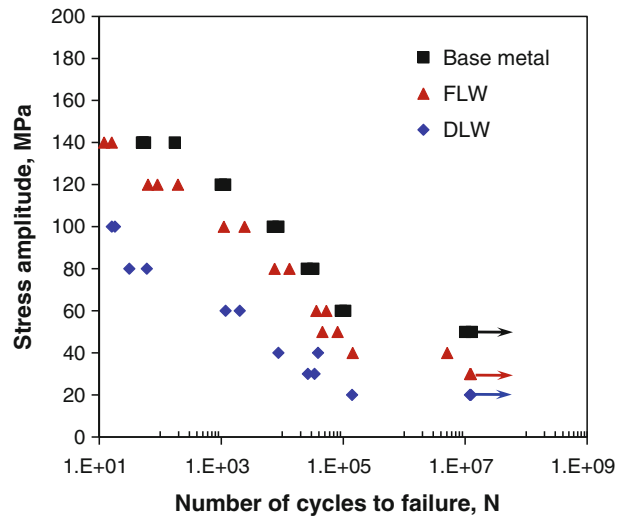
Table II. Ultimate Tensile Strength, Fatigue Limit and Fatigue Ratio of the AZ31B-H24 Mg BM, FLW, and DLW Joints

Specimen	Fatigue Limit (MPa)	Ultimate Tensile Strength (MPa)	Fatigue Ratio
Base metal	50	285	0.175
FLW	30	260	0.115
DLW	20	169	0.118

corresponding to 1×10^7 cycles) and calculated fatigue ratio (the ratio of the fatigue limit to the ultimate tensile strength) of the BM and laser-welded joints are listed in Table II.

The fatigue limit of the FLW and DLW joints dropped by 40 pct and 60 pct, respectively, and the fatigue ratio for both types of laser-welded joints decreased by approximately 34 pct compared with that of the BM. This was attributed mainly to the microstructural change after welding, as illustrated in Figures 3 and 4. In addition, the geometry and shape of the DLW joints were another important factor responsible for the considerable decrease in the fatigue life (Figure 13). The presence of the weld drop through in the FZ of the DLW joints (Figure 4(a)) would result in an extra bending moment. This would facilitate the early fatigue crack initiation and subsequent propagation at the center of the weld drop through in the DLW joints, as indicated by A in Figure 4(a), thus giving rise to a significantly reduced fatigue strength or fatigue life of the DLW joints (Figure 13).The following Basquin-type equation[56] could be used to fit the obtained fatigue data

$$\sigma_a = \sigma'_f (2N_f)^b \qquad [6]$$

where σ_a is the cyclic stress amplitude, σ'_f is the fatigue strength coefficient defined by the stress intercept at

$2N_f = 1$, N_f is the number of cycles to failure, $2N_f$ is the number of reversals to failure, and b is the fatigue strength exponent. The obtained σ_f' and b values are listed in Table III. Fatigue life was indeed associated with both the fatigue strength exponent (b) and the fatigue strength coefficient (σ_f') based on Eq. [6]. Normally, a smaller value of b corresponded to a longer fatigue life.[56] From Table III, it can be observed that the values (including the minus sign) of the fatigue strength exponent were in the following sequence (from low to high): DLW joints < FLW joints < BM. If only the fatigue strength exponent were considered, the DLW joints would have a longer fatigue life. However, a big difference exists in the fatigue strength coefficient where the highest value was obtained for the BM and the lowest for the DLW joints, with the σ_f' value of the FLW joints laying in-between those of the BM and DLW joints. This suggested that Basquin-type equation could be used to describe the fatigue life of welded Mg joints.

Table III. Fatigue Strength Coefficient σ_f' and Fatigue Strength Exponent b of the AZ31B-H24 Mg Base Metal, Flwed and Dlwed Joints

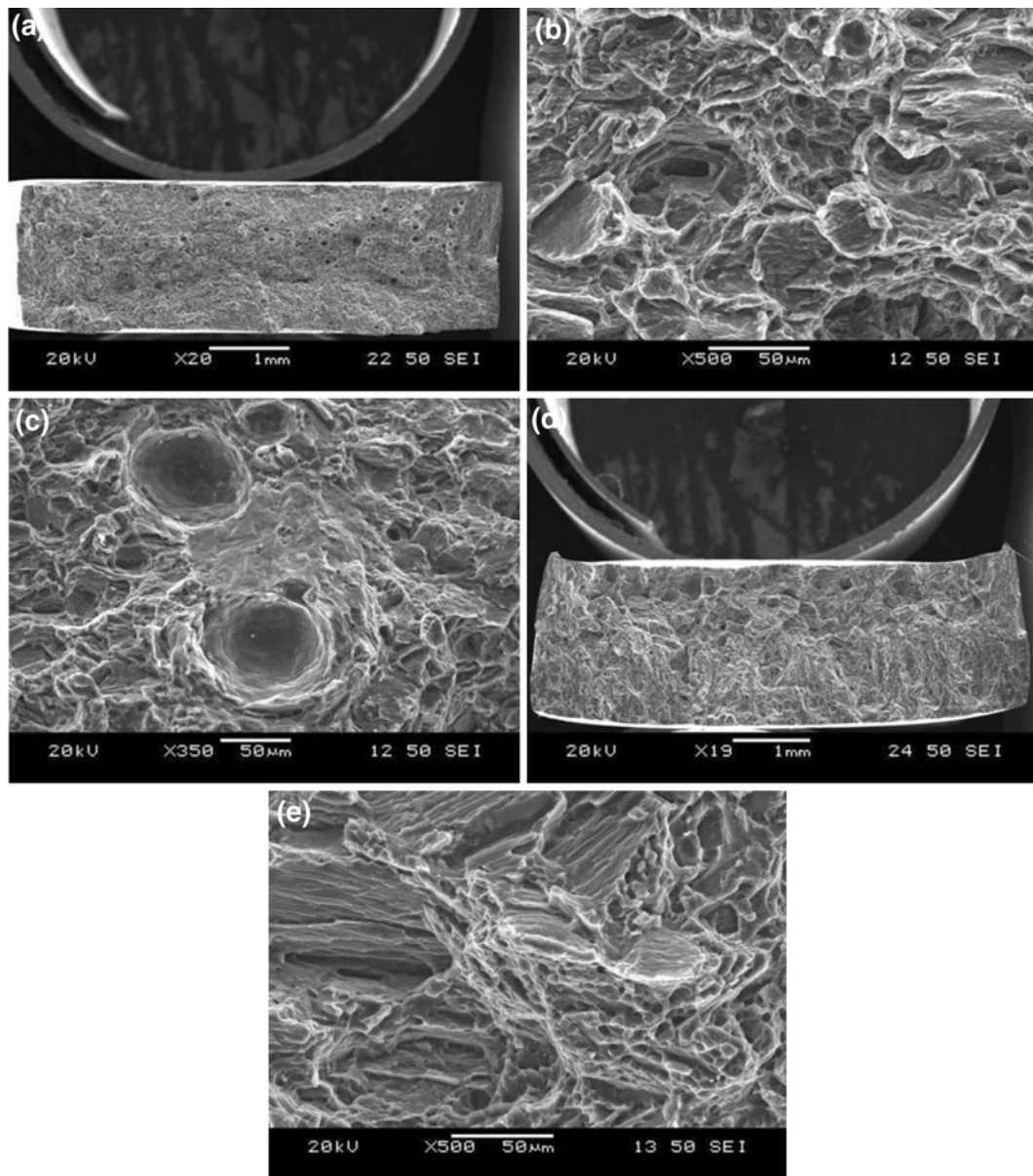| Specimen	σ_f' (MPa)	b
Base metal	274	−0.115
FLW	218	−0.121
DLW	153	−0.133

Fig. 14—Typical SEM images showing the fracture surfaces after tensile testing at a strain rate of 1×10^{-5} s^{-1}, (a) overall view of the entire fracture surface and (b) and (c) magnified view at higher magnifications of a FLW sample, (d) overall view of the entire fracture surface, and (e) magnified view at a higher magnification of a DLW sample.

F. Fractography

SEM examinations revealed that dimple-like ductile fracture characteristics appeared in the BM, whereas some cleavage-like flat facets together with dimples and river marking were observed in the welded samples. Figure 14 shows some typical SEM images of fracture surfaces of FLW and DLW samples after tensile tests at a strain rate of 1×10^{-5} seconds^{-1}. First, gas pores were more obvious in the FLW samples than in the DLW samples, as observed from Figures 14(a) through (c), leading to the decrease of ductility (pct El). Cleavage-like brittle fracture characteristics, *i.e.*, some flat facets in conjunction with river marking, appeared in both the welded samples as shown in Figures 14(b), (c), and (e). The river marking was caused by the crack moving through the grains along several crystallographic planes that formed a series of plateaus and connecting ledges.[56] The fractographic observations corresponded well to the relatively low percent elongation of 5 to 6 pct in the welded samples (Figures 9 and 10(c)).

Figures 15 and 16 show typical SEM images taken from the fatigue fracture surface of FLW and DLW joints, respectively. Fatigue crack basically initiated from the near-surface welding defect (Figures 15(a) and (c)) or from the surface (Figures 16(a) and (b)). Welding defects or shrinkage pores were observed in both types of laser-welded joints (Figures 15(c) and 16(b)). Multiple crack initiation sites were more apparent at higher stress amplitudes as observed from Figure 15(b). In the absence of surface welding defects (*e.g.*, Figure 15(b)), surface grains were usually less constrained than the interior grains, and the occurrence of slip in a few grains near the specimen surface could become relatively easier during fatigue.[57] Surface roughness and protrusions could also act as a site of stress concentration that caused the crack initiation during fatigue. Fatigue crack propagation was characterized mainly by fatigue striations (Figures 15(d) and 16(d)) along with secondary cracks, which were usually perpendicular to the propagating direction. The fatigue striations normally occurred by a repeated plastic blunting-sharpening process in the face-centered cubic materials because of the slip of dislocations in the plastic zone ahead of the fatigue crack tip. The formation of the fatigue striations in the magnesium alloys with a hexagonal close-packed crystal structure was expected to be related to the twinning in the compressive phase and detwinning in the tensile phase.[58–62] Subsequent studies are needed in this aspect.

IV. CONCLUSIONS

1. The microstructure of the as-received AZ31B-H24 Mg alloy consisted of small elongated grains, with some Mn-Al–containing inclusions that were still present in different zones after laser welding. Both DLW and FLW resulted in a typical
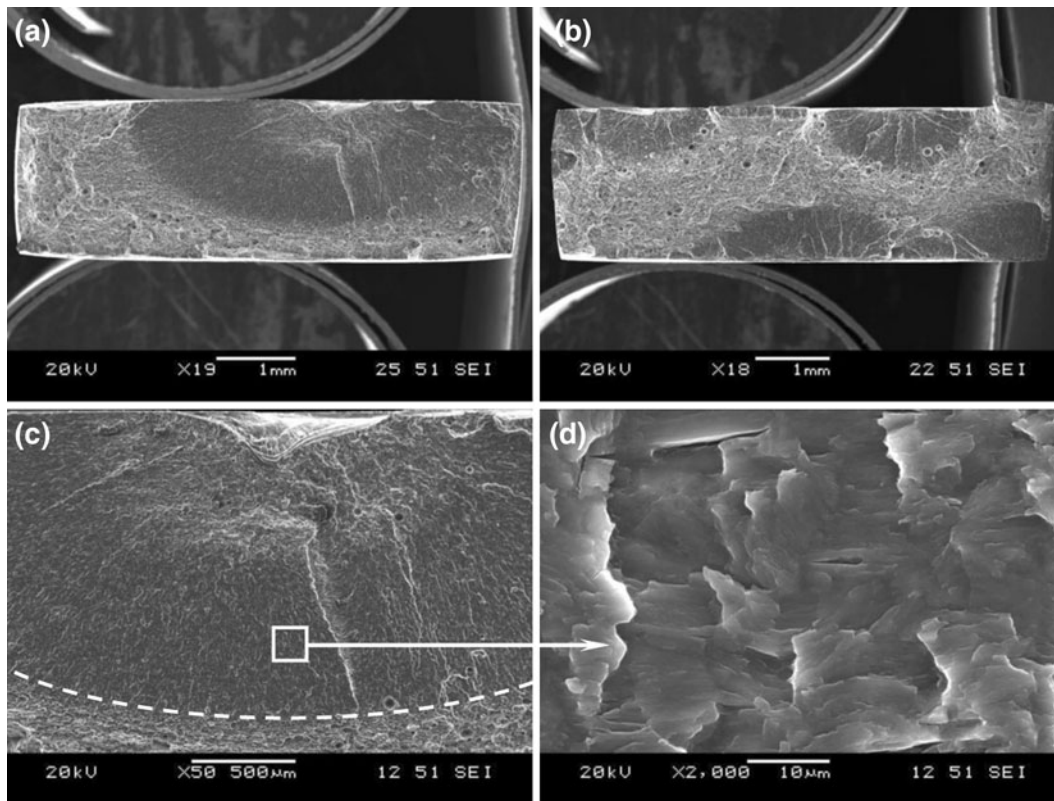

Fig. 15—Typical SEM images of fatigue fracture surface of FLW joints. (*a*) overall view of the entire fracture surface at a lower stress amplitude of 40 MPa, (*b*) multiple crack initiation at a higher stress amplitude of 80 MPa, (*c*) crack initiation from a welding defect, and (*d*) crack propagation zone.
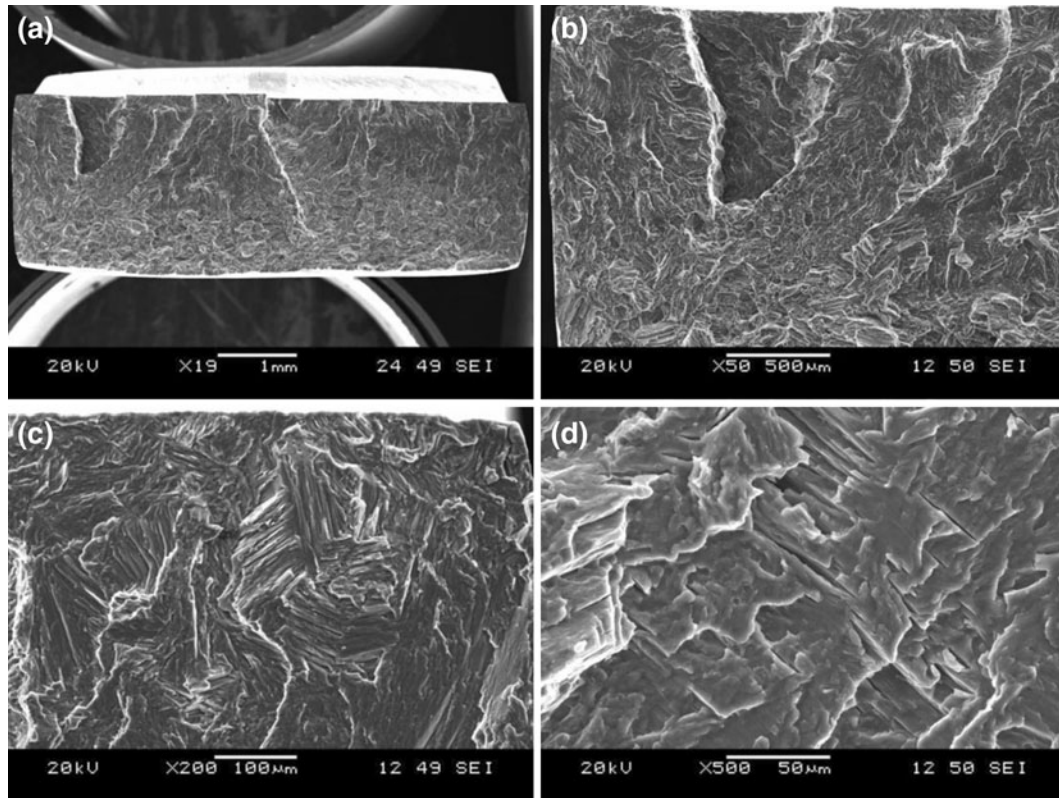
Fig. 16—Typical SEM images of fatigue fracture surface of a DLW joint tested at a stress amplitude of 40 MPa. (*a*) Overall view of the entire fracture surface at a low magnification, (*b*) welding defect at a higher magnification, (*c*) crack initiation site at a higher magnification, and (*d*) crack propagation zone at a higher magnification.

solidification dendritic structure in the fusion zone FZ, coupled with a large number of divorced eutectic β-$Mg_{17}Al_{12}$ particles in the interdendritic and intergranular regions, whereas recrystallized grains appeared in the HAZ.

2. In both types of laser-welded joints, columnar dendrites were observed near the fusion boundary, whereas equiaxed dendrites occurred at the center of the FZ. In comparison with the DLW joints, the FLW joints were superior because the weld sagging/drop-through was absent, the FZ was narrower, and the dendrite cell/grain size was smaller as a result of the higher cooling rate and faster welding speed.

3. After laser welding, the hardness of the AZ31B-H24 Mg alloy decreased, and the lowest value occurred in the FZ. Because of the smaller grain size in the FZ, the FLW joints exhibited a higher hardness than the DLW joints.

4. Although the YS, UTS, and fatigue strength of the DLW joints became much lower because of the larger dendrite cell size and the presence of weld drop through in the FZ, the decrease of the YS, UTS, and fatigue strength in the FLW joints was moderate. Indeed, the FLW led to a joint efficiency of approximately 91 pct because of the narrower FZ, smaller grain size, and absence of weld drop through in the FZ. However, the ductility after both types of laser welding decreased drastically.

5. Although the strain rate dependence of ductility was observed to be strong in the BM, the YS and UTS exhibited only a weak strain rate dependence. After welding, the strain rate sensitivity basically disappeared. Besides, the DLW led to a higher strain-hardening capacity becauase of the softer FZ stemming from the larger grain size.

6. An initially higher strain-hardening rate in the BM at lower net flow stresses was observed because of smaller and predeformed grains where dislocations had been generated, coupled with stronger Hall-Petch contribution arising from smaller grain sizes. At higher net flow stresses, the strain-hardening rate of the welded joints became higher because of the larger grains, providing more space to accommodate dislocations and increasing the dislocation storage capacity.

7. In the tensile and fatigue tests, all the FLW joints basically fractured at the fusion boundary between HAZ and columnar dendrites, whereas the DLW joints fractured almost exclusively at the center of the FZ because of the large dendrite cell size and the presence of weld drop through. Dimple-like ductile fracture characteristics appeared in the BM, whereas some cleavage-like flat facets together with dimples and river marking were observed in the welded samples. The gas pores on the fracture surface of the FLW joints were observed as a result of the keyhole welding process.

8. Fatigue crack initiation occurred from the specimen surface or near-surface welding defects in all the welded joints. Multiple crack initiation was observed at higher stress amplitudes. Fatigue crack propagation was characterized by the formation of fatigue striations with the spacing increased with increasing distance from the initiation site, along with the presence of secondary cracks.

REFERENCES

1. T.M. Pollock: *Science*, 2010, vol. 328, pp. 986–87.
2. M. Wise, K. Calvin, A. Thomson, L. Clarke, B. Bond-Lamberty, R. Sands, S.J. Smith, A. Janetos, and J. Edmonds: *Science*, 2009, vol. 324, pp. 1183–86.
3. L.R. Kump: *Nature*, 2002, vol. 419, pp. 188–90.
4. J.A. Patz, D. Campbell-Lendrum, T. Holloway, and J.A. Foley: *Nature*, 2005, vol. 438, pp. 310–17.
5. E.A. Nyberg, A.A. Luo, K. Sadayappan, and W.F. Shi: *Adv. Mater. Process.*, 2008, vol. 166, pp. 35–37.
6. S.R. Agnew: *JOM*, 2004, vol. 56, pp. 20–21.
7. E.S. Ng and I.A. Watson: *J. Laser Appl.*, 1999, vol. 11, pp. 273–78.
8. P.S. Mohanty and J. Mazumder: *Metall. Mater. Trans. A*, 1998, vol. 45A, pp. 1269–79.
9. S. Kou and Y. Le: *Metall. Trans. A*, 1985, vol. 16A, pp. 1887–96.
10. M. Rappaz, J.M. Vitek, S.A. David, and L.A. Boatner: *Metall. Trans. A*, 1993, vol. 24A, pp. 1433–46.
11. K. Somboonsuk, J.T. Mason, and R. Trivedi: *Metall. Trans. A*, 1984, vol. 15A, pp. 967–75.
12. S.H. Wu, J.C. Huang, and Y.N. Wang: *Metall. Mater. Trans. A*, 2004, vol. 35A, pp. 2455–69.
13. Y. Liu, J. Koch, J. Mazumder, and K. Shibata: *Metall. Trans. B*, 1994, vol. 25B, pp. 425–34.
14. Q. Yajie, Z. Chen, Z. Yu, X. Gong, and M. Li: *Mater. Charact.*, 2008, vol. 59, pp. 1799–804.
15. L. Yu, K. Nakata, N, Yamamoto, and J. Liao: *Mater. Lett*, 2009, vol. 63, pp. 870–72.
16. Z.H. Yu, H.G. Yan, X.S. Gong, Y.J. Quan, J.H. Chen, and Q. Chen: *Mater. Sci. Eng. A*, 2009, vol. A523, pp. 220–25.
17. A. Weisheit, R. Galun, and B.L. Mordike: *Weld. J.*, 1998, vol. 77, pp. 149–54.
18. H. Zhao and T. DebRoy: *Weld. J.*, 2001, vol. 80, pp. 204–10.
19. Z. Sun, D. Pan, and J. Wei: *Sci. Technol. Weld. Join.*, 2002, vol. 7, pp. 343–51.
20. G. Padmanaban and V. Balasubramanian: *Mater. Des.*, 2010, vol. 31, pp. 3724–32.
21. H. Sun, G. Song, and L.F. Zhang: *Sci. Technol. Weld. Join.*, 2008, vol. 13, pp. 305–11.
22. S. Katayama, H. Nagayama, M. Mizutani, and Y. Kawahito: *J. Light Met. Weld. Construct.*, 2008, vol. 46, pp. 470–79.
23. L. Quintino, A. Costa, R. Miranda, D. Yapp, V. Kumar, and C.J. Kong: *Mater. Des.*, 2007, vol. 28, pp. 1231–37.
24. J. Liu, J.H. Dong, and K. Shinozaki: *Mater. Sci. Forum*, 2009, vol. 610-3, pp. 911–14.
25. L. Yu, K. Nakata, and J. Liao: *Sci. Technol. Weld. Join.*, 2009, vol. 14, pp. 554–58.
26. G.F. Vander Voort: *Metallography Principles and Practice*, ASM International, Materials Park, OH, 1999.
27. ASTM Standard E8/E8M: 2008, "Standard Test Methods for Tension Testing of Metallic Materials," ASTM International, West Conshohohocken, PA, 2008.
28. American Welding Society, *Welding Handbook*, 7th ed., vol. 1, American Welding Society, Miami, FL, 1976.
29. X.Z. Lin and D.L. Chen: *J. Mater. Eng. Perform.*, 2008, vol. 17, pp. 894–901.
30. W.F. Savage, C.D. Lundin, and A.H. Aronson: *Weld. J.*, 1965, vol. 44, pp. 175–81.
31. L. Xiao, L. Liu, Y. Zhou, and S. Esmaeili: *Metall. Mater. Trans. A*, 2010, vol. 41A, pp. 1511–22.
32. L. Liu, L. Xiao, J.C. Feng, Y.H. Tian, S.Q. Zhou, and Y. Zhou: *Metall. Mater. Trans. A*, in press.
33. A. Munitz: *Metall. Trans. B*, 1985, vol. 16B, pp. 149–61.
34. A.J. Paul and T. Debroy: *Rev. Mod. Phys.*, 1995, vol. 67, pp. 85–112.
35. S. Kou and Y. Le: *Metall. Trans. A*, 1982, vol. 13A, pp. 1141–52.
36. T.S. Plaskett and W.C. Winegard: *Can. J. Appl. Physiol*, 1960, vol. 38, pp. 1077–88.
37. S. Kou: *Welding Metallurgy*, 2nd ed., Wiley, New York, NY, 2003.
38. Y. Kawahito, M. Mizutani, and S. Katayama: *Trans. JWRI.*, 2007, vol. 36, pp. 11–16.
39. L.M. Liu, G. Song, and M.L. Zhu: *Metall. Mater. Trans. A*, 2008, vol. 39A, pp. 1702–11.
40. P. Liu, Y.J. Li, H.R. Geng, and J.A. Wang: *Mater. Lett.*, 2007, vol. 61, pp. 1288–91.
41. S.F. Su, J.C. Huang, H.K. Lin, and N.J. Ho: *Metall. Mater. Trans. A*, 2002, vol. 33A, pp. 1461–73.
42. G. Padmanaban, V. Balasubramanian, and J.K. Sarin Sundar: *JMPEG*, 2010, vol. 19 (2), pp. 155–65.
43. S.M. Chowdhury, D.L. Chen, S.D. Bhole, X. Cao, E. Powidajko, D.C. Weckman, and Y. Zhou: *Mater. Sci. Eng. A*, 2010, vol. A527, pp. 2951–61.
44. J.A. del Valle and O.A. Ruano: *Scripta Mater*, 2006, vol. 55, pp. 775–78.
45. Y.V.R.K. Prasad and R.W. Armstrong: *Phil. Mag.*, 1974, vol. 29, pp. 1421–25.
46. H. Takuda, S. Kikuchi, N. Yoshida, and H. Okahara: *Metall. Mater. Trans. A*, 2003, vol. 44A, pp. 2266–70.
47. Y.M. Wang and E. Ma: *Mater. Sci. Eng. A*, 2004, vols. A375–A377, pp. 46–52.
48. J. Luo, Z. Mei, W. Tian, and Z. Wang: *Mater. Sci. Eng. A*, 2006, vol. A441, pp. 282–90.
49. N. Afrin, D.L. Chen, X. Cao, and M. Jahazi: *Scripta Mater.*, 2007, vol. 57, pp. 1004–07.
50. J.H. Hollomon: *Trans. AIME*, 1945, vol. 162, pp. 268–89.
51. J.A. del Valle, F. Carreno, and O.A. Ruano: *Acta Mater*, 2006, vol. 54, pp. 4247–59.
52. C.W. Sinclair, W.J. Poole, and Y. Brechet: *Scripta Mater.*, 2006, vol. 55, pp. 739–42.
53. W. Pantleon: *Mater. Sci. Eng. A*, 2004, vols. A387–A389, pp. 257–61.
54. I. Kovacs, N.Q. Chinh, and E. Kovacs-Csetenyi: *Phys. Status Solidi A*, 2002, vol. 194, pp. 3–18.

55. U.F. Kocks and H. Mecking: *Prog. Mater. Sci.*, 2003, vol. 48, pp. 171–273.
56. G.E. Dieter: *Mechanical Metallurgy*, S.I. Metric, ed., McGraw-Hill Columbus, OH, 1988.
57. K.S. Chan, P. Yi-Ming, D. Davidson, and R.C. McClung: *Mater. Sci. Eng. A*, 1997, vol. A222, pp. 1–8.
58. S. Begum, D.L. Chen, S. Xu, and A.A. Luo: *Metall. Mater. Trans. A*, 2008, vol. 39A, pp. 3014–26.
59. L. Wu, A. Jain, D.W. Brown, G.M. Stoica, S.R. Agnew, B. Clausen, D.E. Fielden, and P.K. Liaw: *Acta Mater.*, 2008, vol. 56, pp. 688–95.
60. X.Y. Lou, M. Li, R.K. Boger, S.R. Agnew, and R.H. Wagoner: *Int. J. Plast.*, 2007, vol. 23, pp. 44–86.
61. S. Begum, D.L. Chen, S. Xu, and A.A. Luo: *Int. J. Fatigue*, 2009, vol. 31, pp. 726–35.
62. S. Begum, D.L. Chen, S. Xu, and A.A Luo: *Mater. Sci. Eng. A*, 2009, vol. A517 (1–2), pp. 334–43.